

Complex-domain super-resolution imaging with distributed optimization

Xuyang Chang¹, Liheng Bian^{1,*}, Shaowei Jiang², Guoan Zheng², and Jun Zhang¹

¹*School of Information and Electronics & Advanced Research Institute of Multidisciplinary Science, Beijing Institute of Technology, Beijing 100081, China.*

²*Department of Biomedical Engineering, University of Connecticut, Storrs, CT, 06269, USA.*

Complex-domain imaging has emerged as a valuable technique for investigating weak-scattered samples. However, due to the detector’s pursuit of large pixel size for high throughput, the resolution limitation impedes its further development. In this work, we report a lensless on-chip complex-domain imaging system, together with a distributed-optimization-based pixel super-resolution technique (DO-PSR). The system employs a diffuser shifting to realize phase modulation and increases observation diversity. The corresponding DO-PSR technique derives an alternating projection operator and an enhancing neural network to tackle the measurement fidelity and statistical prior regularization subproblems. Extensive experiments show that the system outperforms the existing techniques with as much as 11dB on PSNR, and one-order-of-magnitude higher cell counting precision.

Complex-domain images provide both amplitude and phase maps, enabling to conveniently study the intrinsic structure of unstained weak-scattered samples [1]. Generally, in order to maintain high imaging quality with a high signal-to-noise ratio (SNR), most imaging systems require a detector with a large pixel size to acquire enough photons during limited exposure [2]. However, the large pixel size in confined areas results in a decreased imaging resolution with insufficient pixels, which may fail to meet the Nyquist sampling criteria [3], and leads to the loss of important target information [4, 5]. This limitation impedes further development of complex-domain imaging.

Recent advance in computational imaging has suggested that the pixel size limitation can be bypassed computationally by the complex-domain pixel super-resolution (CD-PSR) technique [6–15]. CD-PSR first increases observation diversity by such as sub-pixel shifting [6, 8, 16], wavelength scanning [12], varying illumination angles/heights/distances [7, 17, 18], and amplitude/phase modulation [15, 19]. Observation diversity provides extra information of the latent high-resolution image. The multiple acquisitions are then synthesized to reconstruct more pixels to address the pixel loss of the detector. CD-PSR has been applied in both lens-based projection imaging [20, 21] and lensless holographic imaging [17, 22, 23] systems to enhance imaging resolution.

Particularly, CD-PSR is required to reconstruct both high-resolution (HR) amplitude and phase from low-resolution (LR) intensity-only measurements. Mathematically, the forward measurement model is

$$y = |\mathbf{A}u|^2 + \omega, \quad (1)$$

where u is the latent to-be-reconstructed signal ($u \in \mathbb{C}^{n \times 1}$), y denotes the measurement sequence

($y \in \mathbb{R}^{m \times 1}$), \mathbf{A} represents the undersampled measurement matrix ($\mathbf{A} \in \mathbb{R}^{m \times n}$ or $\mathbb{C}^{m \times n}$), and ω stands for measurement noise.

Most of the conventional CD-PSR techniques are built on the alternating projection technique (AP) [15, 19], which is a generalized phase retrieval framework pioneered by Gerchberg, Saxton and Fienup [24, 25]. Since measurement noise can flow into the to-be-reconstruction signal, AP is not robust against noise. To enhance the reconstruction quality, the super-resolution sparse phase-amplitude retrieval (SR-SPAR) [19] technique introduces non-local self-similarity regularization to attenuate the negative influence of noise, which is of high computational complexity. The adaptive smoothing algorithm has also been applied to CD-PSR (AS-PSR) [15], which utilizes the mean filtering with plenty of hyperparameters to remove measurement noise. Recently, the emerging deep learning technique has also been tried for CD-PSR [14] in a holographic setup. However, deep learning maintains poor generalization and requires new large-scale datasets and retraining for different system configurations or even different element parameters.

In this work, we report a lensless on-chip complex-domain imaging system, together with a distributed-optimization-based pixel super-resolution technique (DO-PSR). In this system, a unit magnification configuration with a Fresnel number of $\sim 50,000$ is employed to realize wide-field imaging. A thin diffuser is placed between the sample and the detector for wavefront modulation. The diffuser is removed from different $x - y$ positions to increase observation diversity for quantitative complex-domain recovery. Benefiting from the powerful reconstruction algorithm and simple imaging system, the reported technique is able to realize high-fidelity complex-domain reconstruction and rapid high-precision image analysis.

The DO-PSR reconstruction takes the advantage of the physics model to impose data fidelity and the deep denoising prior for high running efficiency. Specifically,

* bian@bit.edu.cn

we extend the generalized-alternating-projection (GAP) [26–28] framework from linear real field to nonlinear complex field, and decompose CD-PSR into two sub-problems, including measurement fidelity and statistical prior regularization. These two sub-problems are independent of each other, offering flexible implementation for respective optimization. We introduce an alternating projection operator to tackle the measurement fidelity regularization, due to its strong generalization ability on different imaging modalities. An enhancing neural network is applied to solve the prior regularization, benefiting from its high fidelity and high efficiency. In this way, the reported DO-PSR technique enjoys both operators’ advantages, and brings strong robustness, high efficiency and wide generalization for various CD-PSR settings.

The complex-domain super-resolution imaging modality that employs wavefront modulation to increase observation diversity [29] is shown in Fig.1. The high-resolution target wavefront $u(x, y)$ is first modulated by a series of modulation masks $d_\ell (\ell = 1, 2, \dots)$, and the resulted wavefront $\mathcal{P}_\ell(x, y, 0) = d_\ell \odot u(x, y)$ (\odot denotes the Hadamard product) propagates a distance of z to the detector plane. We utilize the Rayleigh–Sommerfeld diffraction model to describe wavefront propagation [30] as

$$\mathcal{P}_\ell(x, y, z) = \mathcal{F}^{-1} \{ H(f_x, f_y, z) \cdot \mathcal{F}[d_\ell \odot u(x, y)] \}, \quad (2)$$

where \mathcal{F} and \mathcal{F}^{-1} represent Fourier transform (FT) and inverse FT, respectively. $H(f_x, f_y, z)$ is the transfer function defined following the angular spectrum theory as

$$H = \begin{cases} \exp \left[i \frac{2\pi}{\lambda} z \sqrt{1 - \lambda^2 (f_x^2 + f_y^2)} \right], & f_x^2 + f_y^2 \leq \frac{1}{\lambda^2} \\ 0 & \text{otherwise,} \end{cases} \quad (3)$$

where λ is illumination wavelength, and (f_x, f_y) represent spatial frequencies. As the detector acquires only light intensity, the measurement formation model can be summarized as

$$y = |\mathbf{A}u|^2 + \omega, \quad (4)$$

where \mathbf{A} represents the above modulation, propagation and undersampling process. Assuming that the detector pixel size is $\theta_D \times \theta_D$, and that of the high-resolution target is $\theta_C \times \theta_C$, the following introduced CD-PSR reconstruction engages to solve the problem of $\theta_D > \theta_C$.

The reported DO-PSR technique models the general CD-PSR optimization as

$$\hat{u} = \arg \min_u f(u) + \lambda g(u), \quad (5)$$

where $f(u)$ is a data-fidelity regularizer that ensures consistency between the reconstructed result and measurements, and $g(u)$ is a regularizer that imposes certain prior constraints. Since the minimum value of Eq.(5) is the saddle point of its augmented Lagrangian function, by introducing an auxiliary variable v to approximate u , the

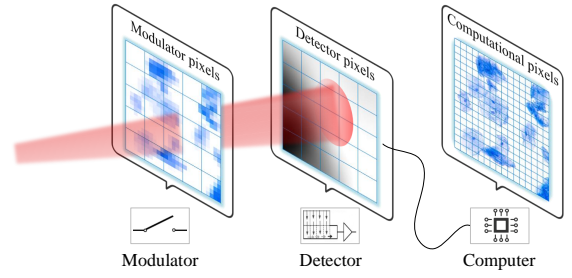


FIG. 1. Illustration of the super-resolution framework. After wavefront modulation, the target wavefront is undersampled with insufficient detector pixels. By employing the computational reconstruction technique, the high-resolution complex-domain target can be retrieved with more pixels.

objective function can be rewritten using the generalized-alternating-projection strategy [26] as

$$(u, v) = \underset{y = |\mathbf{A}u|^2}{\operatorname{argmin}} 1/2 \|u - v\|_2^2 + g(v). \quad (6)$$

Eq. (6) is solved by alternatively and iteratively optimizing the following two subproblems.

Solving u : given $v^{(j)}$, $u^{(j+1)}$ is updated via a Euclidean projection of $v^{(j)}$ on the manifold $y = |\mathbf{A}u|^2$ as

$$u^{j+1} = v^{(j)} + \eta \cdot \text{PSR}(y - \beta \cdot |\mathbf{A}v|^2), \quad (7)$$

where η and β are weight coefficients, and PSR denotes the pixel super-resolution solver to regularize measurement fidelity.

Considering that the alternating projection reconstruction method maintains low computational complexity [31], we derive the PSR solver following the AP strategy. Specifically, the object wavefront starts with a random HR initialization, and propagates to the imaging plane after modulation. We assume that each $\theta \times \theta$ pixel patch in the HR wavefront corresponds to one pixel in the captured LR intensity-only image. Consequently, each measurement is applied to update the total intensity of the corresponding pixel patch, following the fifth line in Algorithm S1 (Supplement Material). Then the updated HR wavefront is back propagated to the object plane to obtain updated $u^{(j+1)}$.

Solving v : given $u^{(j+1)}$, $v^{(j+1)}$ is updated by an image enhancing regularizer as

$$v^{j+1} = \text{EN}(u^{j+1}). \quad (8)$$

As suggested by the development of computer vision in recent years, the reconstruction quality of an image can be enhanced by imposing prior constraints, such as total variation [32] and non-local self-similarity [33]. We first employ total variation as the regularizer to demonstrate the effectiveness, termed as DOTV-PSR. Then, considering that the deep learning technique maintains high inference efficiency and enhancing quality, we further employ the state-of-the-art FFDNET [34] as the enhancing regularizer (DONet-PSR). The FFDNET is a convolutional

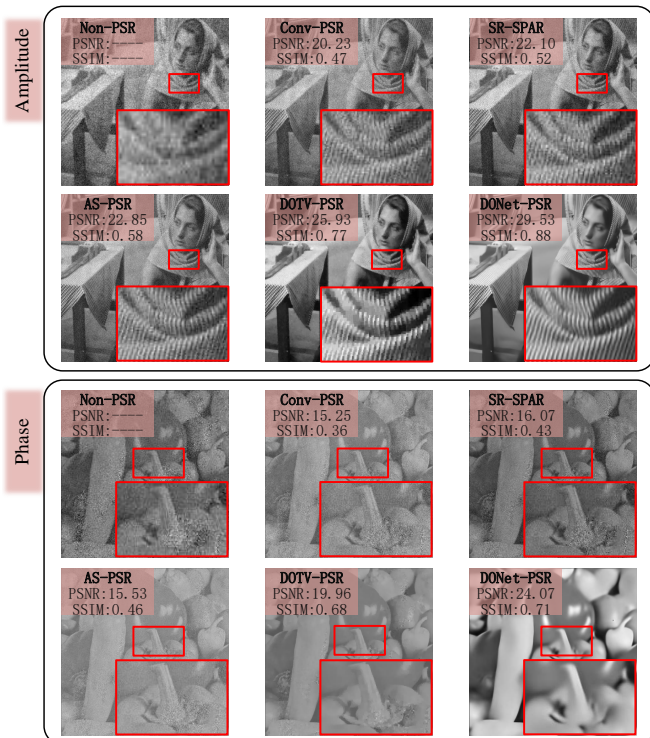


FIG. 2. Comparison of different CD-PSR algorithms under shot noise (Poisson distribution), with undersampling factor $\theta = 2$. The acquired images without PSR obtain a low resolution, and the shot noise further degrades imaging quality. Using CD-PSR, the resolution is enhanced. However, the conventional PSR techniques still suffer from corrupted measurement noise. The reported DO-PSR technique enables effective noise removal while reserving structure details. The results of $\theta = 3, 4$ are shown in Fig. S3 (Supplementary Material).

neural network that provides flexible and fast solutions under various noise levels, which make a great tradeoff between noise suppression and detail fidelity.

The complete DO-PSR algorithm is summarized in Algorithm S1 (Supplement Material). After initializing the variables and parameters, DO-PSR iteratively updates u and v following Eq. (7) and Eq. (8) in an alternative manner (keeping one fixed while updating the other one). The hyper-parameters β and η control the convergence rate of the AP solver. The demo code has been released at bianlab.github.io.

We compare the reported techniques (DOTV-PSR and DONet-PSR) against the existing state-of-the-art CD-PSR algorithms on synthetic data at first, to investigate their performance under various system settings. The competing algorithms include the conventional PSR (Conv-PSR) [7], the super-resolution sparse phase-amplitude retrieval (SR-SPAR) [19] and the recent reported adaptive smoothing PSR (AS-PSR) [15]. The illumination wavelength was $532nm$, and the propagation distance between the image plane and detector plane was $21.55mm$. The detector's pixel size was $1.4\mu m$.

First, we study these algorithms' performance under

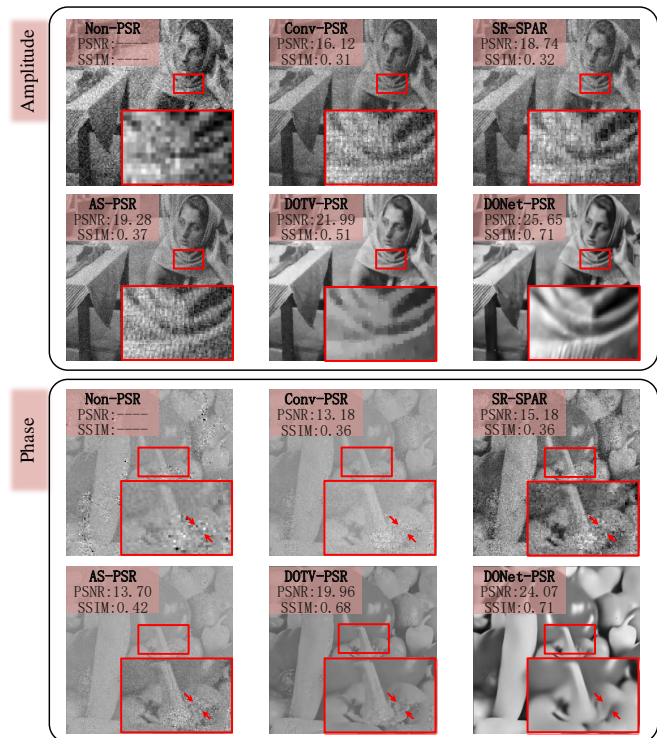


FIG. 3. Comparison of different CD-PSR algorithms under Gaussian noise, with SNR = 2 and undersampling factor $\theta = 4$. The reported DO-PSR technique outperforms other techniques and is able to effectively recover the cross-talk in the phase and amplitude (as indicated by the red arrows in the phase images). The results of other noise levels and undersampling factors are shown in Tab. S1, Figs. S4, S5 and S6 (Supplementary Material).

different modulation times and explore their convergence. The undersampling factor θ is fixed to 3. Figure S2 (Supplementary Material) presents the quantitative comparison of both amplitude and phase. Since the PSNR of most algorithms increases slowly as the mask number is more than 60, we fixed the mask number to 60 in the following simulations.

Then, we study the impact of measurement noise on reconstruction quality. We first added shot noise to measurements, which describes the random arrival of particle-like light and follows the Poisson distribution. Figure 2 shows the reconstruction results of different CD-PSR techniques with the undersampling factor $\theta = 2$ (The results of $\theta = 3, 4$ are shown in Fig. S3 (Supplementary Material)). We can see that as the undersampling factor θ increases, the imaging quality of Non-PSR degrades due to insufficient sampling and noise corruption. Although the conventional CD-PSR methods (Conv-PSR, SR-SPAR and AS-PSR) enable enhancing imaging resolution, they still suffer from noise degradation. The background is not smooth and the structural details are buried in measurement noise. In contrast, the reported DO-PSR technique obtains the best imaging quality for both amplitude and phase. As validated by the close-ups

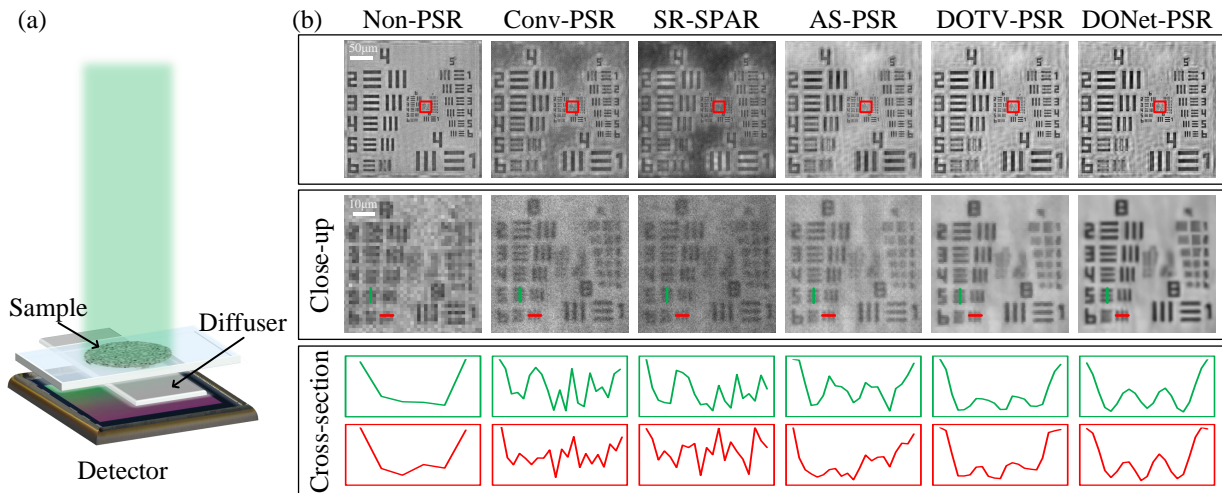


FIG. 4. Experiments results of different CD-PSR methods on a USAF target. (a) is the schematic of the lensless on-chip microscopy system. (b) shows the reconstruction results and close-up of different algorithms. Non-PSR obtains a low resolution, with a lot of fine details lost. The other CD-PSR algorithms (Conv-PSR, SR-SPAR and AS-PSR) suffer from poor noise robustness, which produces low fidelity. In comparison, DO-PSR outperforms with a higher imaging resolution and smooth background.

of the scarf and peduncle, it efficiently attenuates noise while preserving fine details. Quantitatively, it maintains as much as 9.3dB and 8.8dB enhancement on PSNR for amplitude and phase, and as much as 0.46 and 0.40 increase on SSIM over the conventional methods.

Next, to investigate the PSR techniques under different noise levels, we added white Gaussian noise of different SNR to measurements. Figure 3 shows the reconstruction results under extreme noise SNR = 2dB and undersampling factors $\theta = 4$. Table S1, Figures S4, S5 and S6 (Supplementary Material) shows the quantitative and visual results of other different undersampling factors and noise levels. For Conv-PSR, noise level maintains more influence on reconstruction quality than downsampling factor. By introducing sparsity prior and adaptive gradient, the SR-SPAR and AS-PSR methods enable to improve reconstruction quality to some extent. In comparison, the reported DO-PSR technique maintains the strongest robustness to both noise levels and downsampling factors. It obtains as much as 11dB and 10dB enhancement on PSNR for amplitude and phase respectively, and as much as 0.5 and 0.28 on SSIM.

Then, we built a DIY lensless on-chip microscopy system, together with the DO-PSR algorithm to demonstrate rapid complex-domain super-resolution imaging and intelligent processing. The system cost less than 100 dollars (except light source and detector) and its prototype is presented in Fig. 4 (a) and Fig. S1 (Supplementary Material). The setup includes a fiber-coupled diode as light source (532nm, 5mW), a coverslip coated with $\sim 1\mu\text{m}$ polystyrene beads placed in between the sample and the detector as a diffuser to implement wavefront modulation, and a detector with $1.67\mu\text{m}$ pixel size (MT9J003 ON Semiconductor). The distance between

sample and detector is $\sim 1\text{mm}$. The Fresnel number is $\sim 50,000$ which is calculated by imaging area divided 'distance-wavelength'. The large Fresnel number means little diffraction from the sample plane to the detector plane. We set the diffuser to be moved different 225 $x - y$ positions to realize modulation diversity. We captured three groups of LR measurements of different samples, including a USAF resolution test chart, a mouse kidney slide and a U87MG cell culture. The mask calibration and sample preparation methods are described in the supplementary material.

Figure 4 (b) presents the reconstruction results of the USAF target. Due to limited resolution, the Non-PSR method can not produce enough fine details in close-ups. It can only resolve the features of group 7, element 5. Although the conventional PSR methods obtain resolution enhancement which can resolve the features of group 8, element 5, they are disturbed by measurement noise due to limited exposure. In contrast, the reported DO-PSR technique enables the recovery of higher resolution (group 8, element 6) with smooth background.

Figure 5 presents the reconstructed phase images of two unstained tissue samples, including a mouse kidney slide and a U87MG cell culture. We can see that the results without PSR maintain an ambiguous cellular outline. The conventional PSR techniques enable to enhance resolution, but the image contrast is still unsatisfactory with disturbing noise and aberrations. In contrast, the reported DO-PSR technique produces high-fidelity results that effectively preserve fine details while attenuating unpleasant artifacts. Besides, DO-PSR is able to successfully recover high-density areas (as indicated by the arrows in close-ups), which indicate the potential cell overlap in three dimensions. The wide-field reconstruc-

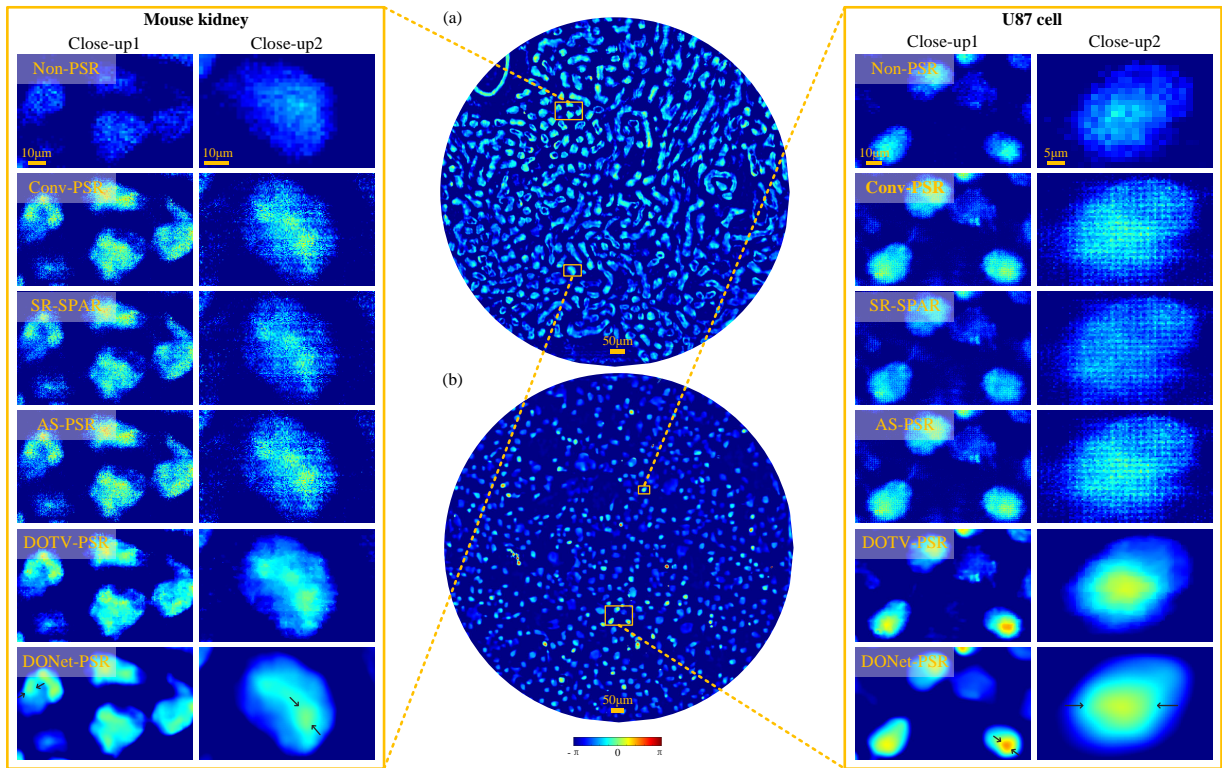


FIG. 5. Comparison of different CD-PSR techniques on phase targets. (a) and (b) are the reconstructed mouse kidney slide and U87MG cell culture using DO-PSR. The close-ups of different methods show that Non-PSR lose lots of details due to limited resolution, and the other CD-PSR algorithms produce reconstruction artifacts with low image contrast. The reported DO-PSR obtains state-of-the-art results, with high-fidelity cell morphology and smooth background.

TABLE I. The results of cell counting. There are 70 cells in the selected region via manual counting. The reported DONet-PSR obtains one-order-of-magnitude higher counting precision than the other CD-PSR algorithms.

Algorithms	Cell number	Error
Conv-PSR	89	27.14%
SR-SPAR	96	37.14%
AS-PSR	89	27.14%
DOTV-PSR	83	18.57%
DONet-PSR	72	2.86%

tion results of different techniques are presented in supplementary material: Figs. S8 and S9.

The state-of-the-art performance of the DO-PSR technique and low-cost rapid imaging platform benefit for subsequent image analysis and intelligent processing. As a demonstration, we employed the watershed algorithm [35] to implement cell segmentation and counting on the reconstructed images of U87 cell culture. Specifically, we selected a $\sim 350\mu\text{m} \times 350\mu\text{m}$ square region, and binarized the images to separate the U87 cells from the background. After image filling, we employed watershed transform to perform cell segmentation. The marginal cells were removed to eliminate counting errors.

Figure 6 presents the segmentation results of U87 cells.

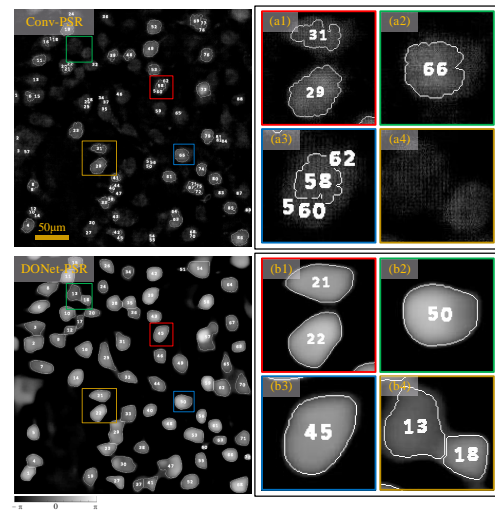


FIG. 6. The segmentation results of U87 cells. We employed the watershed algorithm to segment the reconstructed images of different CD-PSR techniques. The unpleasant reconstruction quality of the conventional PSR methods makes it hard for them to process the overlapping or connective cells, leading to incorrect segmentation or even omissive counting (see close-ups). In comparison, the segmentation result of DO-PSR is more accurate.

We can see that the Conv-PSR can not produce smooth segmentation edges. In comparison, the reported DO-PSR technique enables even segmentation, as shown in the close-ups (a1)-(a2) and (b1)-(b2). Furthermore, there are quite a few cells that are wrongly segmented (a3) or even undetected (a4) by Conv-PSR, while the reported DO-PSR technique produces high-fidelity results. Table I shows the cell counting results. For the selected $\sim 350\mu\text{m}^2$ region, there is an average of 70 cells via manual counting by three persons. We can see that the counting result of DONet-PSR is most close to manual counting with only 2.86% counting error, which is one-order-of-magnitude higher than the other PSR algorithms. In summary, the unpleasant reconstruction quality of the conventional PSR techniques makes automatic cell segmentation challenging. The DO-PSR technique is able to produce a clear cell structure and achieve an effective

solution for rapid label-free cell segmentation. The complete results of cell segmentation and counting are presented in Fig. S10 (supplementary material).

To conclude, we focus on complex-domain super-resolution imaging, and reported a lensless on-chip complex-domain imaging system, together with an efficient distributed-optimization-based pixel super-resolution technique. Extensive experiments demonstrate the effectiveness of the reported technique with the ability of wide-field high-resolution complex-domain imaging and one-order-of-magnitude higher image analysis precision.

This work was supported by the National Natural Science Foundation of China (Nos. 61971045, 61827901, 61991451), National Key R&D Program (Grant No. 2020YFB0505601), Fundamental Research Funds for the Central Universities (Grant No. 3052019024).

-
- [1] Y. Park, C. Depeursinge, and G. Popescu, *Nat. Photonics* **12**, 578 (2018).
- [2] R. Hain, C. J. Kähler, and C. Tropea, *Experiments in fluids* **42**, 403 (2007).
- [3] G. Zheng, R. Horstmeyer, and C. Yang, *Nat. Photonics* **7**, 739 (2013).
- [4] D. J. Brady, M. E. Gehm, R. A. Stack, D. L. Marks, D. S. Kittle, D. R. Golish, E. Vera, and S. D. Feller, *Nature* **486**, 386 (2012).
- [5] J. Fan, J. Suo, J. Wu, H. Xie, Y. Shen, F. Chen, G. Wang, L. Cao, G. Jin, Q. He, *et al.*, *Nat. Photonics* **13**, 809 (2019).
- [6] M. Ben-Ezra, A. Zomet, and S. K. Nayar, *IEEE T. Pattern Anal.* **27**, 977 (2005).
- [7] X. Hu, S. Li, and Y. Wu, *Appl. Optics* **47**, 6079 (2008).
- [8] W. Bishara, T.-W. Su, A. F. Coskun, and A. Ozcan, *Opt. Express* **18**, 11181 (2010).
- [9] W. Bishara, U. Sikora, O. Mudanyali, T.-W. Su, O. Yaglidere, S. Luckhart, and A. Ozcan, *Lab Chip* **11**, 1276 (2011).
- [10] A. Greenbaum and A. Ozcan, *Opt. Express* **20**, 3129 (2012).
- [11] A. C. Sobieranski, F. Inci, H. C. Tekin, M. Yuksekkaya, E. Comunello, D. Cobra, A. Von Wangenheim, and U. Demirci, *Light: Sci. Appl.* **4**, e346 (2015).
- [12] W. Luo, Y. Zhang, A. Feizi, Z. Göröcs, and A. Ozcan, *Light: Sci. Appl.* **5**, e16060 (2016).
- [13] J. Zhang, J. Sun, Q. Chen, J. Li, and C. Zuo, *Sci. Rep.* **7**, 1 (2017).
- [14] Z. Luo, A. Yurt, R. Stahl, A. Lambrechts, V. Reumers, D. Braeken, and L. Lagae, *Opt. Express* **27**, 13581 (2019).
- [15] Y. Gao and L. Cao, *Opt. Letters* **45**, 6807 (2020).
- [16] M. Elad and A. Feuer, *IEEE T. Image Process.* **6**, 1646 (1997).
- [17] W. Luo, A. Greenbaum, Y. Zhang, and A. Ozcan, *Light: Sci. Appl.* **4**, e261 (2015).
- [18] G. Zheng, S. A. Lee, Y. Antebi, M. B. Elowitz, and C. Yang, *P. Natl. Acad. Sci. USA* **108**, 16889 (2011).
- [19] V. Katkovnik, I. Shevkunov, N. V. Petrov, and K. Egiazarian, *Optica* **4**, 786 (2017).
- [20] S. C. Park, M. K. Park, and M. G. Kang, *IEEE Signal Proc. Mag.* **20**, 21 (2003).
- [21] S. Farsiu, M. Elad, and P. Milanfar, *IEEE T. Image Process.* **15**, 141 (2005).
- [22] A. Greenbaum, W. Luo, T.-W. Su, Z. Göröcs, L. Xue, S. O. Isikman, A. F. Coskun, O. Mudanyali, and A. Ozcan, *Nat. Methods* **9**, 889 (2012).
- [23] A. Greenbaum, Y. Zhang, A. Feizi, P.-L. Chung, W. Luo, S. R. Kandukuri, and A. Ozcan, *Sci. Transl. Med.* **6**, 267ra175 (2014).
- [24] R. W. Gerchberg, *Optik* **35**, 237 (1972).
- [25] J. R. Fienup, *Appl. Optics* **21**, 2758 (1982).
- [26] X. Liao, H. Li, and L. Carin, *SIAM J. Imaging Sci.* **7**, 797 (2014).
- [27] X. Yuan, in *International Conference on Image Processing (ICIP)* (IEEE, 2016) pp. 2539–2543.
- [28] X. Yuan, Y. Liu, J. Suo, and Q. Dai, in *Conference on Computer Vision and Pattern Recognition (CVPR)* (2020) pp. 1447–1457.
- [29] E. J. Candes, X. Li, and M. Soltanolkotabi, *Appl. Comput Harmon. A.* **39**, 277 (2015).
- [30] J. W. Goodman, (Roberts and Company Publishers, 2005).
- [31] Y. Shechtman, Y. C. Eldar, O. Cohen, H. N. Chapman, J. Miao, and M. Segev, *IEEE Signal Proc. Mag.* **32**, 87 (2015).
- [32] L. I. Rudin, S. Osher, and E. Fatemi, *Physica D* **60**, 259 (1992).
- [33] Z. Kong, X. Yang, and L. He, *arXiv preprint arXiv:2011.03462* (2020).
- [34] K. Zhang, W. Zuo, and L. Zhang, *IEEE T. Image Process.* **27**, 4608 (2018).
- [35] J. B. Roerdink and A. Meijster, *Fund. Inform.* **41**, 187 (2000).